Capillarity

Vol. 16, No. 2, p. 39-50, 2025

Original article

Experimental investigation and multi-scale simulations of CO_2 foam flooding for enhanced oil recovery

Mingguo Peng[1,2], Yan Zhou[1], Jun Yang[1], Jun Wang[3], Zeyu Lin[4], Jing Zhao[1]*

[1]*School of Petroleum and Natural Gas Engineering, School of Energy, Changzhou University, Changzhou 213164, P. R. China*

[2]*Jiangsu Provincial Engineering Center for Oil & Gas Low-Carbon Development and New Energy Integrated Utilization, Changzhou 213164, P. R. China*

[3]*Oil & Gas Technology Research Institute of Changqing Oilfield Company, Xi'an 710018, P. R. China*

[4]*Research Institute of Petroleum Exploration and Development, PetroChina, Beijing 100089, P. R. China*

Keywords:
CO_2 foam flooding
enhanced oil recovery
pore network modeling
reservoir simulation

Cited as:
Peng, M., Zhou, Y., Yang, J., Wang, J., Lin, Z., Zhao, J. Experimental investigation and multi-scale simulations of CO_2 foam flooding for enhanced oil recovery. Capillarity, 2025, 16(2): 39-50.
https://doi.org/10.46690/capi.2025.08.02

Abstract:
CO_2 flooding in low-permeability and tight oil reservoirs is frequently compromised by severe gas channeling, which significantly reduces oil recovery and sweep efficiency. While foam flooding can effectively mitigate CO_2 channeling by trapping CO_2 within lamellae, its stability deteriorates under harsh high-temperature, high-salinity reservoir conditions, compromising its effectiveness. Furthermore, foam flow in porous media involves constant foam generation, collapse and propagation, making its flow behaviors difficult to predict. To address these challenges, a new foaming agent with satisfactory regenerative capability is developed to maintain gas mobility control under harsh reservoir conditions. The multiphase flow behaviors during CO_2 foam flooding are predicted using pore network modeling to obtain the corresponding relative permeability curves, which are further incorporated into a reservoir simulator to evaluate field-scale foam flooding performances, as well as optimize injection strategies. This multi-scale modeling approach establishes a quantitative link between pore-scale foam behaviors and field-scale oil recovery performances, offering new insights into carbon capture and utilization with enhanced oil recovery in low-permeability and tight reservoirs.

1. Introduction

Low-permeability and tight reservoirs are characterized by low porosity, strong heterogeneity, and insufficient nature energy (Li et al., 2021; Ji and Fang, 2023). CO_2 flooding demonstrates significant potential for enhancing oil recovery in these formations by reducing oil viscosity and lowering Interfacial Tension (IFT) (Hamza et al., 2021; Prakash et al., 2024; Rahman et al., 2024). Furthermore, this technique aligns with carbon capture and utilization initiatives, offering the dual benefits of improving oil recovery and mitigating the greenhouse effect, thereby contributing to energy sustainability (Xu et al., 2022; Yang et al., 2023b; Lin et al., 2024). However, gas fingering frequently occurs during CO_2 flooding in low-permeability and tight reservoirs, significantly compromising sweep efficiency (Kumar and Mandal, 2017).

CO_2 foam flooding has been identified as a promising alternative to mitigate gas channeling by effectively blocking high-permeability zones (Zhang et al., 2025) and trapping gas *in-situ*. The formation of foam increases the apparent viscosity of gas, allowing for a more uniform displacement, and delaying gas breakthrough (Youssif et al., 2024; Chen et

Yandy Scientific Press

---

*Corresponding author.
E-mail address: pmg@cczu.edu.cn (M. Peng); S23040857031@smail.cczu.edu.cn (Y. Zhou); yangjun@cczu.edu.cn (J. Yang); wangj297_cq@petrochina.com.cn (J .Wang); zlo217@petrochina.com.cn (Z. Lin); maggiezhao@cczu.edu.cn (J. Zhao).

Received April 19, 2025; revised May 12, 2025; accepted June 9, 2025; available online June 15, 2025.

al., 2025). The performance of CO_2 foam flooding is highly dependent on foam stability under harsh reservoir conditions (Zhang et al., 2019, 2021). However, conventional polymers, typically incorporated to enhance foam stability, are prone to degradation and often cause poor injectivity due to the narrow pore-throat sizes inherent to low-permeability formations, significantly limiting their field application. Consequently, novel foaming agents are urgently required to sustain foam stability while ensuring good injectivity.

CO_2 foam flooding is a complex dynamic process involving continuous foam generation, collapse, and propagation. This complexity makes accurately predicting multiphase flow behaviors challenging. Key flow parameters, such as relative permeability and capillary pressure curves, are essential inputs for commercial reservoir simulators (Rasmussen et al., 2019; Cai et al., 2023; Zhao et al., 2023a). At present, these parameters are largely derived from empirical correlations, compromising the accuracy of numerical models. Pore Network Modeling (PNM) has emerged as a predictive tool for digital core analysis (Blunt et al., 2013). By integrating scanning electron microscopy with super-resolution techniques, PNM reconstructs realistic pore structures, simplifies porous media representation, and enables efficient prediction of multiphase flow behaviors (Meakin and Tartakovsky, 2009).

Currently, PNM integrated with percolation theory is commonly used to investigate foam characteristics. Laidlaw et al. (1993) emphasized that foam blockage drives the pore network toward the percolation threshold, where significant permeability reduction occurs during foam flow. Kharabaf and Yortsos (1998) employed a simplified PNM and introduced the Invasion Percolation with Memory (IPM) algorithm to identify minimum-threshold pathways enabling foam transport under sufficient pressure gradients. Chen et al. (2005) subsequently modified the IPM to incorporate viscous effects present during flow initiation. Building on this, Zhao et al. (2023b) proposed the Dynamic Invasion Percolation with Memory (DIPM) theory, accounting for the viscous effects induced by lamella viscosity, interfacial deformation, and the Marangoni effect. They then employed PNM coupled with the DIPM algorithm to simulate foam transport in porous media.

To address the above challenges of CO_2 foam flooding in low-permeability and tight reservoirs, this study develops a thermally stable, oil-resistant foaming agent with regenerative capability. Based on this, a multi-scale modeling framework is constructed to optimize CO_2 foam flooding in such formations, comprising two integrated components: (1) A pore-scale simulation platform that combines PNM with the DIPM algorithm to predict key flow parameters and (2) a reservoir-scale numerical model incorporating these parameters for field-scale optimization. This integrated framework quantitatively links pore-scale foam dynamics with field-scale oil recovery, advancing strategies to optimize gas injection efficiency.

2. Experimental section

2.1 Synthesis of foaming agent

To address the challenges of the harsh reservoir conditions, a novel foaming agent Regenerable and Optimized-Stability Enhanced (RO-SE) is developed for CO_2 foam flooding to enhance mobility control. The basic reservoir properties are summarized in Table 1. Synthetic brine with a total salinity of 11,618.7 mg/L is prepared by dissolving inorganic salts (e.g., NaCl) in deionized water to mimic formation water (Table 2). All chemicals are purchased from Shanghai Macklin Biochemical Technology Co. Ltd, China. Crude oil with the viscosity and density of 7.79 MPa·s and 0.82 kg/m^3, respectively, is obtained from Jiangsu oilfield, China.

Table 1. Basic reservoir properties.

Property	Value
Permeability (mD)	16.46
Porosity (%)	13.16
Temperature (°C)	101
Initial gas-oil ratio	93
Initial reservoir pressure (MPa)	28.75
Minimum miscibility pressure (MPa)	31.64

Table 2. Chemical compositions of the formation water.

Ion type	Concentration (mg/L)
$K^+ + Na^+$	3,918.28
Ca^{2+}	54.91
Mg^{2+}	5.35
Cl^-	2,976.4
$SO_4{}^{2-}$	2,967.4
$HCO_3{}^-$	1,696.36

2.2 Characterization of the foaming performances

The RO-SE foam system, consisting of 0.1 wt% fatty alcohol polyoxyethylene ether sulfonate, 0.3 wt% cocoamidopropyl hydroxysultaine betaine, and 0.015 wt% lauryl alcohol, demonstrates strong regeneration performance in low-permeability and tight reservoirs. The foaming properties of the RO-SE foam system are systematically evaluated. Key metrics including foamability, foam stability, and regenerability are assessed and compared with other 2 commercial foaming agents SF1 and SF2.

50 mL of foaming agent is stirred at 3,000 rpm for 3 min using a Waring Blender method (Zhou et al., 2025). The resulting foam is immediately transferred into a 250 mL graduated cylinder, which is then sealed to minimize evaporation. All experiments are conducted at 101 °C to replicate reservoir conditions. Initial foam volume (V_f) is recorded as a measure of foaming capability. Foam stability is assessed by the foam half-life time ($t_{1/2}$), defined as the time required for the foam volume to decrease to half of its initial value. Bulk foam tests are also conducted at different crude oil concentrations to evaluate the performances of different

Table 3. Scanning parameters of the digital core sample.

Parameter	Value
Depth (m)	2,961.9-3,065.3
Permeability (mD)	1.34
Scan size (nm)	$2,900\times 2,900\times 2,100$
Analytical dimension (nm)	$1,007\times 1,007\times 1,007$
Resolution (μm)	3

Table 4. Pseudo-component properties in oil characterization.

Pseudo-component	Mole fraction (%)
C_3-C_6	9.31
C_7-C_{34}	90.69

foaming agents. The Foam Composite Index (FCI) evaluates the comprehensive performance of foam is given by:

$$\mathrm{FCI}=\frac{3}{4}V_f t_{1/2} \tag{1}$$

2.3 Characterization of interfacial properties

2.3.1 Interfacial tension measurement

The pendant drop method is used to determine the equilibrium water/gas IFT (σ). The experiments are performed on instrument interfacial rheometer and the shape of the drop is fitted by high-resolution camera. The drop profile is automatically fitted using image analysis software, and the IFT is calculated based on the Young-Laplace equation. The experiments are performed at temperature of 101 °C and at least 3 times measurements for each solution are carried out.

2.3.2 Interfacial dilational modulus measurements

The interfacial dilational modulus (ε) is determined by measuring the change in stress due to the change in interfacial area of an interface (Ravera et al., 2010). It is measured by imposing a sinusoidal oscillation to the surface area of a pendant drop. The pendant drop is periodically deformed to induce cyclic changes in surface area, with an oscillation amplitude of 10% and frequency of 0.2 Hz. The IFT response is recorded. Experimental temperature is maintained at 101 °C to simulate reservoir conditions, the interfacial dilatational modules is given by:

$$\varepsilon=\frac{A\mathrm{d}\sigma}{\mathrm{d}A} \tag{2}$$

where $\mathrm{d}\sigma$ is the change in IFT, mN/m; A is the mean area of the sinusoidal disturbance, m^2.

3. Model development

3.1 Construction of pore network

High-resolution micro-CT imaging is used to extract the complex pore structure of cores (Table 3). Based on this, the maximum ball method is employed to construct a ball-and-stick model (Roslin et al., 2020). This method defines the maximal balls as the largest spheres centered at each voxel that fit within the pore space, while throats are composed of spheres that decrease in diameter to connect two maximal balls or a group of adjacent spheres equal in size. A subsequent clustering algorithm categorized pores and throats by grouping maximal balls according to size and rank to preserve geometric accuracy. The DIPM algorithm is incorporated into PNM to predict dynamic foam flow behaviors, offering insights into foam flow properties at the micro-scale (Zhao et al., 2023b).

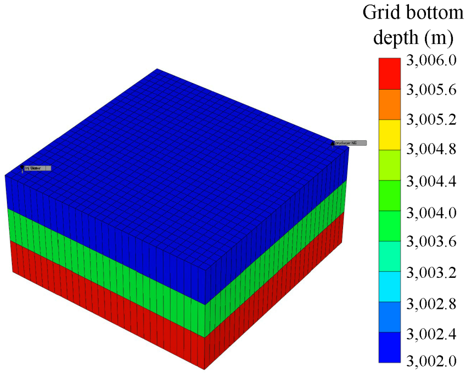

Fig. 1. Three-dimensional concept reservoir model for CO_2 foam flooding.

3.2 Construction of reservoir model

A Three-Dimensional (3D) Cartesian grid model with $30\times 30\times 3$ is constructed, representing a simple heterogeneous concept reservoir model. The production well is located in the grid (2, 29, 2), and the injection well is located in the grid (29, 2, 2), as shown in Fig. 1. All the 3 layers are perforated. The pressure and temperature are set at 30 MPa and 101 °C, respectively. The permeability and porosity are set at 10 mD and 10%, and the initial oil saturation is 70%.

3.3 Oil properties and foam dynamic model

Thirty-two components are identified in the oil using gas chromatography. To improve computational efficiency and reduce the complexity of oil component characterization, these components are lumped into 2 pseudo-components, as listed in Table 4, ensuring minimal deviation from the original oil properties. The PVT model incorporates these pseudo-components to describe oil properties under varying pressure and temperature conditions, with key properties such as density and viscosity validated against experimental data for accuracy. This model serves as a basis for reservoir simulation and performance prediction for injection and production scenarios. The principal mechanisms and quantitative chemical reaction formulas governing foam lamella dynamics used in STARS module of CMG simulator (Zhang et al., 2015) are systematically summarized in Table 5.

3.4 Interactive platform development

Relative permeability curves are incorporated into the CMG-STARS simulator through a platform developed using

Table 5. Chemical reaction formulas for foam dynamics model.

Mechanism	Reaction formula
Lamella generation	$9.9995e^{-1}$ Water + $9.2222e^{-5}$ Surfactant + $CO_2 \rightarrow$ Lamella + CO_2
Lamella coalescence	Lamella $\rightarrow 9.995e^{-1}$ Water + $9.522e^{-5}$ Surfactant
Trapped gas release	Foam gas $\rightarrow CO_2$
Lamella collapse in the presence of oil	Lamella + C_7-$C_{34} \rightarrow 9.9995e^{-1}$ Water + $9.222e^{-5}$ Surfactant + C_7-C_{34}
Trapped gas release in the presence of oil	C_7-C_{34} + Foam gas $\rightarrow C_7$-C_{34} + CO_2
Lamella-assisted trapped gas formation	Lamella + $CO_2 \rightarrow$ Lamella + Foam gas

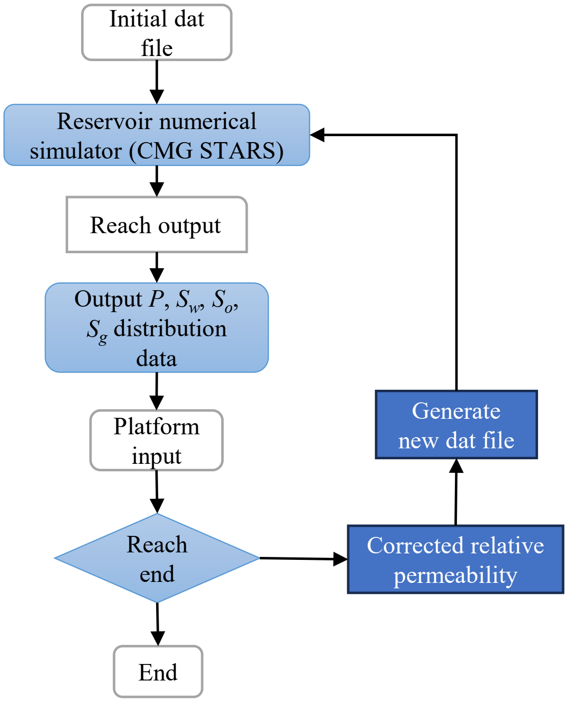

Fig. 2. Numerical simulation flow chart.

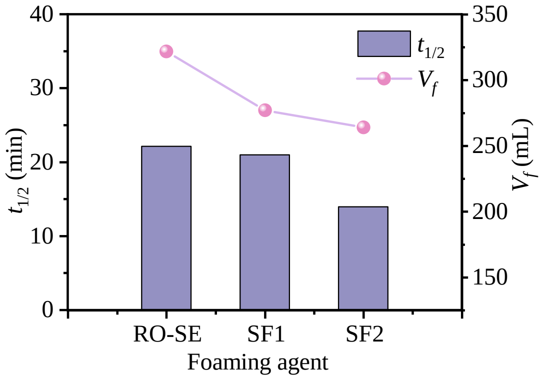

Fig. 3. The initial foam volume (V_f) and half-life time ($t_{1/2}$) of foaming agents.

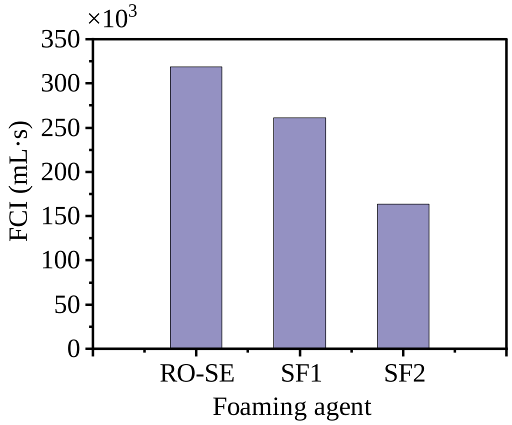

Fig. 4. The FCI of foaming agents.

MATLAB. This platform enables automated reading of STARS simulation results, correction of relative permeability curves, rewriting of STARS input files, and rerunning of simulations. The procedure is composed of the following steps (Fig. 2):

1) For each grid block, relative permeability curves are obtained using pore network modeling, and are exported into CMG-STARS-compatible files.
2) For each grid block, gas relative permeability is corrected according to the local pressure.
3) Generating STARS input files based on the corrected relative permeability data.
4) When STARS module runs to the designated step, local pressure (P), water saturation (S_w), oil saturation (S_o), gas saturation (S_g), and saturation history within the grid are output.
5) The relative permeability data for each grid is updated based on the output data obtained using pore network modeling.
6) The corrected data is compiled into new files and reintroduced into the STARS module.
7) Steps 4)-6) are repeated iteratively until the simulation is complete.

4. Results and discussion

4.1 Foaming performance of foaming agents

The V_f, $t_{1/2}$, and FCI of different foaming agents are shown in Figs. 3 and 4. Under reservoir conditions, foam performance varies significantly among the tested systems. The RO-SE foam system exhibits the highest V_f of 322 mL, demonstrating superior foaming ability. Its $t_{1/2}$ is 22 min, slightly longer than that of SF1 foam system, indicating relatively good foam stab-

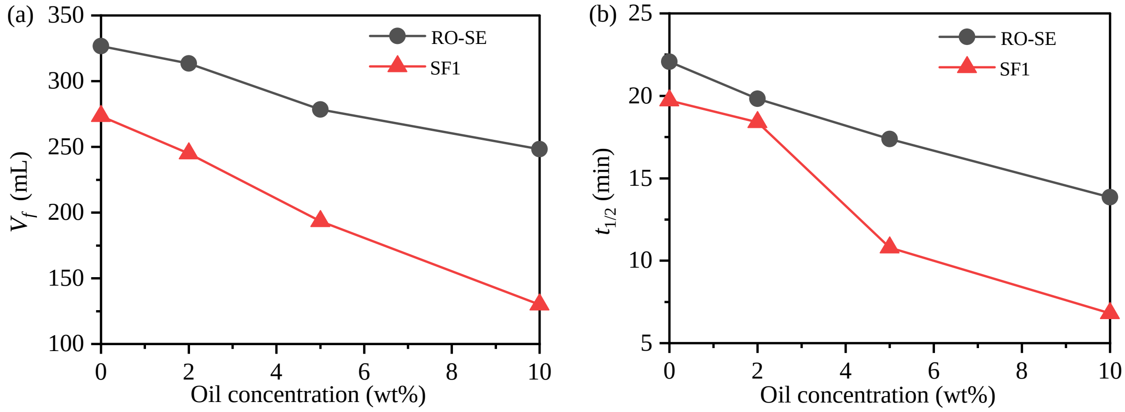

Fig. 5. Foam performance under different oil concentrations: (a) Initial foam volume (V_f) and (b) half-life time ($t_{1/2}$).

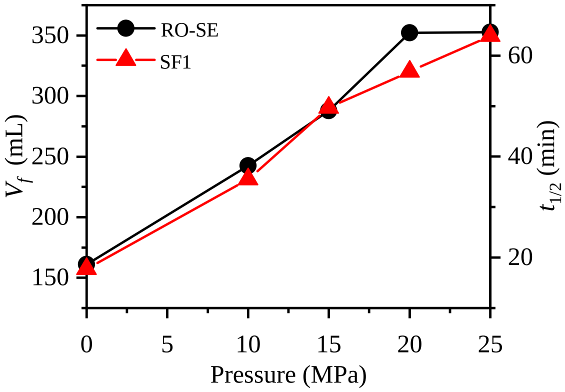

Fig. 6. Initial foam volume (V_f) and half-life time ($t_{1/2}$) of the foam systems under different pressures.

ility. It is observed that the SF2 foam system collapses rapidly, with a much shorter $t_{1/2}$ of 14 min, reflecting poor foam stability. Meanwhile, the RO-SE foam system also exhibits a significantly higher FCI value of 318,780 mL·s, compared to only 163,800 mL·s for SF2 foam system. Consequently, RO-SE foam system offers an effective combination of foaming capacity and stability compared to other 2 foaming agents, making it a promising candidate for field application.

The V_f and $t_{1/2}$ of RO-SE and SF1 foam systems in the presence of oil at different concentrations are presented in Figs. 5(a) and 5(b). Although the presence of oil compromises foam stability, the RO-SE system is less affected, reflecting its higher oil tolerance. For instance, as the oil concentration increases to 10 wt%, the V_f and $t_{1/2}$ of the SF1 foam system decrease by approximately 65% and 52%, respectively, compared to 0 wt%, while the RO-SE foam system shows smaller reductions of about 37% and 24%. The above results show that RO-SE retains stronger foaming ability, stability, and better oil tolerance, underscoring its adaptability in harsh reservoir conditions.

The V_f and $t_{1/2}$ of RO-SE and SF1 foam systems at varying pressures are shown in Fig. 6. The bubble size distribution after an hour is shown in Fig. 7. Under reservoir conditions, increasing pressure enhances the foaming capability and stability of the RO-SE foam system. Bubble size analysis shows that the RO-SE foam system generates smaller and denser bubbles with diameters smaller than 0.75 mm and a bubble density approximately 3 times higher than that of SF1. Studies have demonstrated that smaller bubbles due to their larger specific surface area enhance foam stability and facilitate their penetration into finer pore spaces for improving microscopic displacement efficiency in low-permeability reservoirs. The “Jamin effect” caused by the accumulation of small bubbles effectively blocks high-permeability channels, diverting the subsequent flow to lower-permeability regions, contributing to larger sweep efficiency (Cai et al., 2024; Dubey and Majumder, 2024).

4.2 Interfacial properties of RO-SE

The interfacial properties of CO_2 foam stabilized are shown in Figs. 8 and 9, respectively. The RO-SE foam system exhibits the lowest IFT of 22.9 mN/m, indicating reduced energy requirements for foam generation and enhanced foaming capability. At a temperature of 101 °C and an oscillation frequency of 0.2 Hz, RO-SE also demonstrates the highest interfacial dilational modulus of 37.28 mN/m, surpassing both the SF1 (~28.15 mN/m) and SF2 foam systems (~15.10 mN/m). A higher interfacial dilational modulus suggests stronger resistance to external disturbances and shear, indicating better thermal resistance and stability (Ma et al., 2025). This improvement can be attributed to the synergistic interactions between the sulfonate groups and quaternary ammonium groups in the RO-SE formulation, which enhance interfacial rigidity through combined electrostatic and hydrophobic effects.

4.3 Pore network model simulation results analysis

4.3.1 Pore network construction and geometrical characterization

The construction process of the PNM is shown in Fig. 10, and the geometric characteristics of the pore network are summarized in Table 6. As shown in Fig. 11(a), the pore radius distribution is primarily centered around 10 µm, which is re-

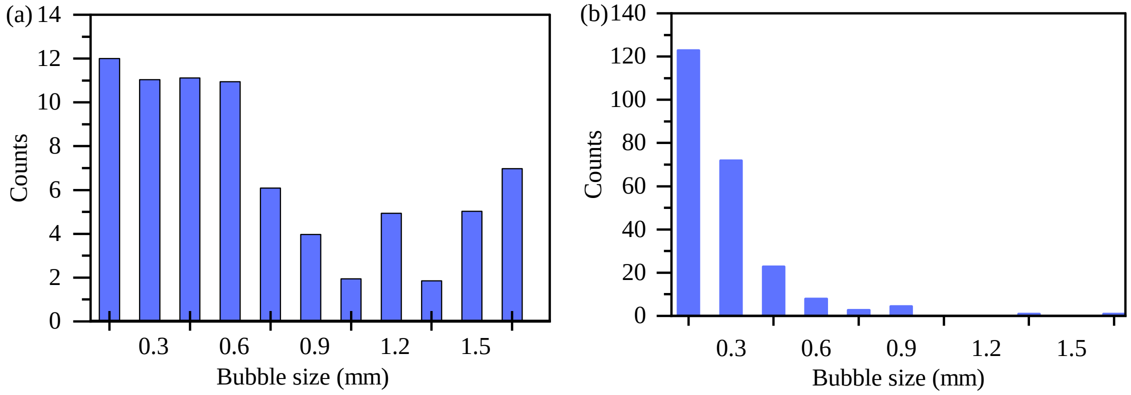

Fig. 7. Bubble size distributions of foam systems for (a) SF1 and (b) RO-SE.

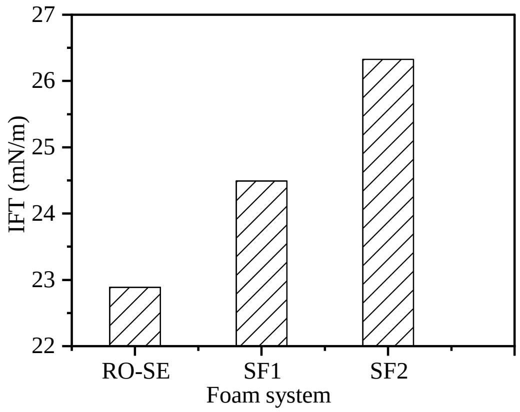

Fig. 8. Interfacial tensions of the foaming agents.

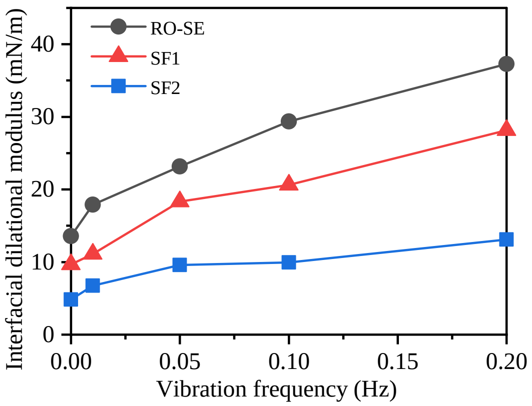

Fig. 9. Interfacial dilational modulus under different vibration frequencies.

presentative of low-permeability reservoirs. The pore throat radii are predominantly around 5 μm (Fig. 11(b)). The narrow pore throats induce high capillary resistance, which hinders foam propagation in the porous media (Cai et al., 2021). Figs. 11(c) and 11(d) indicate that the majority of pores and throats possess low shape factors, especially pore throats, mostly around 0.03, implying irregular geometries (i.e., high heterogeneity) of the network (Qin and van Brummelen, 2019).

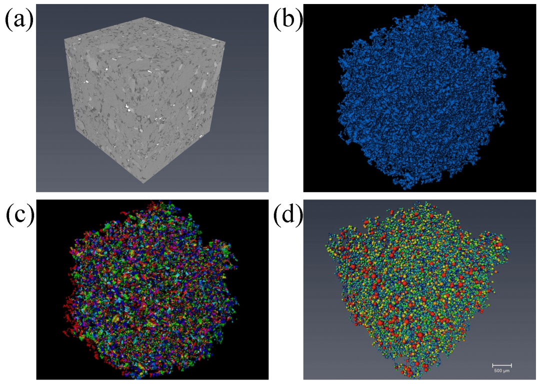

Fig. 10. Construction procedures of digital core: (a) One portion of the core, (b) effective pores after segmentation, (c) effective pore geometry space and (d) the ball-and-stick model.

Table 6. Properties of the pore network modeling.

Parameter	Value	
	Pore	Throat
Count	45,206	67,461
Maximum radius (μm)	57.60	33.95
Mean radius (μm)	8.71	5.02
Maximum volume (μm^3)	2.68×10^6	4.06×10^5
Mean volume (μm^3)	2.10×10^4	8.63×10^3
Maximum coordination number	22	/
Mean coordination number	3.97	/
Maximum length (μm)	/	395
Mean length (μm)	/	22.37

The average coordination number, which reflects the connectivity of the network, is around 3.97, suggesting a moderately well-connected pore network facilitating multi-directional flow (An et al., 2016).

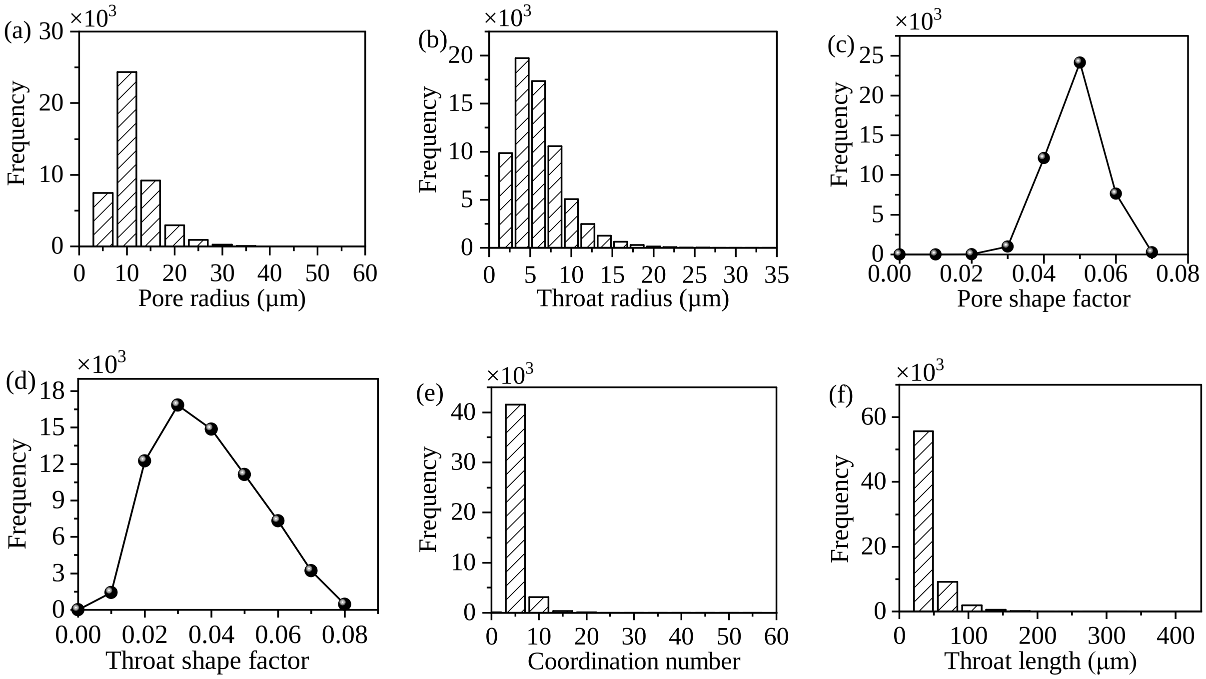

Fig. 11. Characteristics of constructed pore network: (a) Pore radii, (b) throat radii, (c) pore shape factors, (d) throat shape factors, (e) pore coordination numbers and (f) throat lengths.

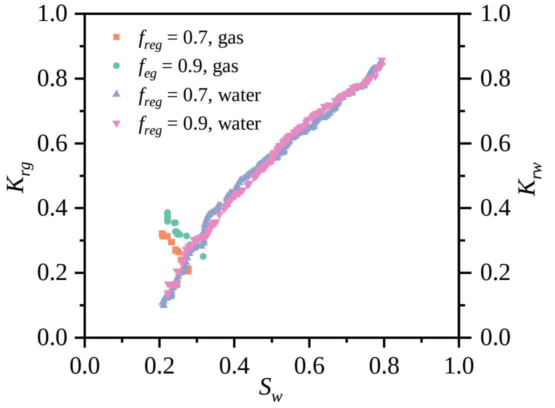

Fig. 12. Relative permeability curves of foam regeneration probabilities.

4.3.2 Relative permeabilities during CO_2 foam flooding

A novel approach is proposed to enhance the prediction accuracy of relative permeability (K_r) curves by integrating the DIPM with the PNM (Zhao et al., 2021; Yang et al., 2023a). By incorporating dynamic pressure regulation and front-velocity calibration, the DIPM algorithm enables real-time tracking of both interfaces of the foam lamella, significantly enhancing the efficiency and accuracy of foam flow prediction. This approach allows rapid, low-cost generation of large-scale foam displacement efficiency datasets. Since foam regeneration probability (f_{reg}) critically influences flow behaviors, it is defined as an input parameter in the DIPM model. As shown in Fig. 12, a higher f_{reg} value of 0.9 leads to increase trapped gas saturation and a reduction in gas relative permeability compared to that of 0.7. As shown in Fig. 13, with a f_{reg} value of 0.8, relative permeability results vary slightly across different flow directions, the overall trend is consistent, directions with better connectivity exhibit lower residual oil saturation. The water phase relative permeability remains low (~ 0.05-0.15), and the residual oil saturation is high (approximately 0.30-0.35), indicating limited mobile oil. A f_{reg} value of 0.8 is used in the simulation due to the strong regenerability of the developed foam system, the CO_2 foam oil/water and gas/water relative permeability curves are thus obtained, where K_{ro}, K_{rw}, and K_{rg} denote the relative permeabilities of oil, water and gas phases, respectively. (Fig. 14).

4.4 Sensitivity analysis

Based on the component inputs, foam reaction mechanisms, and key flow parameters established in previous sections, the model is now fully prepared for subsequent sensitivity analyses. This section focuses on key parameters: Development modes, foam injection timings, injection rates, gas-liquid ratios of the foam slug, and hybrid injection strategies.

4.4.1 Effect of development modes

Oil production rate, oil recovery factor and Gas Oil Ratio (GOR) are compared across the 3 development modes. As shown in Fig. 15(a), gas injection reaches an early peak oil production rate of 10 m^3/day after 0.02 PV of gas injection (i.e. at the very beginning of production), but maintains a very low production rate below 2 m^3/day throughout the rest of the period. When Water Alternating Gas (WAG) injection is

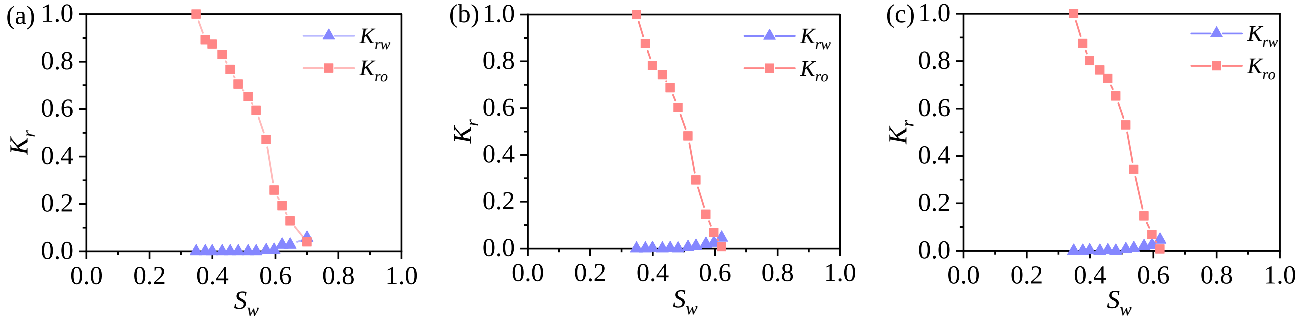

Fig. 13. Relative permeability curves at f_{reg} value of 0.8 in (a) x ($E_d = 0.4973$), (b) y ($E_d = 0.5812$) and (c) z ($E_d = 0.4849$) directions (E_d: Displacement efficiency).

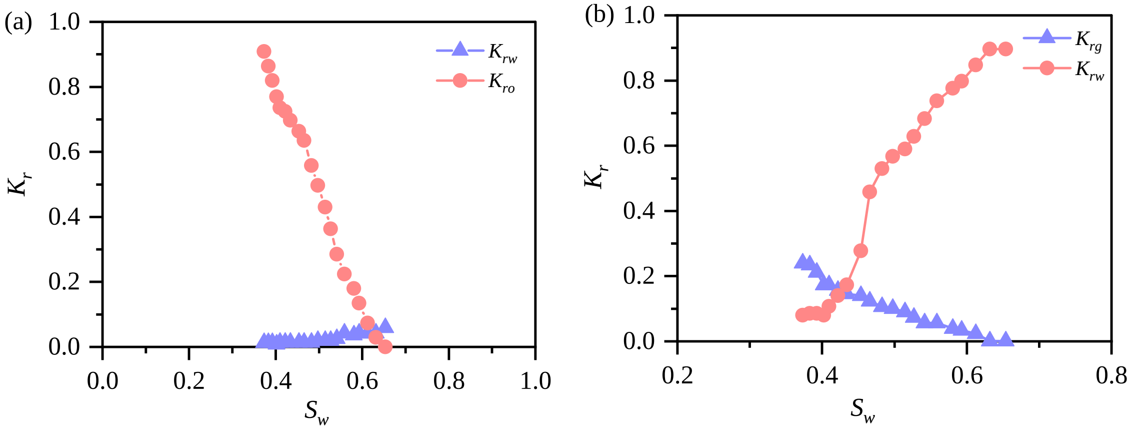

Fig. 14. Relative permeability curves at f_{reg} value of 0.8 predicted by the model: (a) Oil/water and (b) gas/water.

Table 7. Model parameters used for CO_2 foam flooding.

Parameter	Value
Injection rate (m^3/day)	5, 10, 20, 30, 40, 50
Slug number	3
Slug gas-liquid ratio	1 : 1
Injection-production ratio	1 : 1

applied, the oil production rate increases to a higher peak of 15 m^3/day and remains at a relatively high level for over 2 years. Surfactant Alternating Gas (SAG) injection rapidly enhances oil production rate, achieving the highest peak rate of 28 m^3/day and maintaining higher production levels for more than 3 years, indicating superior production performance. As shown in Fig. 15(b), SAG injection achieves the highest ultimate oil recovery factor of 50.06%, significantly outperforming gas injection (∼29%) and WAG injection (∼38.7%). In Fig. 15(c), GOR continuously increases during gas injection. After WAG injection begins, the GOR initially decreases by approximately 34%, while SAG injection immediately reduces the GOR to 0 following injection and maintains this level for approximately 3 years, demonstrating the superior gas mobility control of the SAG strategy.

4.4.2 Effect of foam injection timings

A sensitivity analysis is performed to evaluate the effect of SAG injection timings, where SAG is initiated after 0.04, 0.06, 0.08 and 0.12 PV of gas injection, respectively. In Fig. 16(a), oil production rates show similar trends across different injection timings: An initial sharp increase in oil production rate followed by a gradual decline. The final oil recovery factors presented in Fig. 16(b), indicate that earlier foam injection leads to earlier oil production, but all cases ultimately achieve a similar recovery factor of approximately 50.2%. In Fig. 16(c), earlier SAG injection leads to an earlier reduction in GOR (e.g., at 0.04 PV), but leads to a final GOR 37.7% higher than that of the case at 0.12 PV. This is because earlier foam injection enhances early gas mobility control but compromises injectivity, whereas delayed injection maintains better injectivity and ultimately achieves similar sweep efficiency.

4.4.3 Effect of injection rates

A sensitivity analysis of injection rates is conducted a year after gas injection (Table 7). As shown in Fig. 17, higher injection rates increase oil production rates, with the maximum rate observed at 50 m^3/day. Fig. 18(a) demonstrates that increasing the injection rate enhances the oil recovery factor and prolongs sustained production. Injection rates of 40

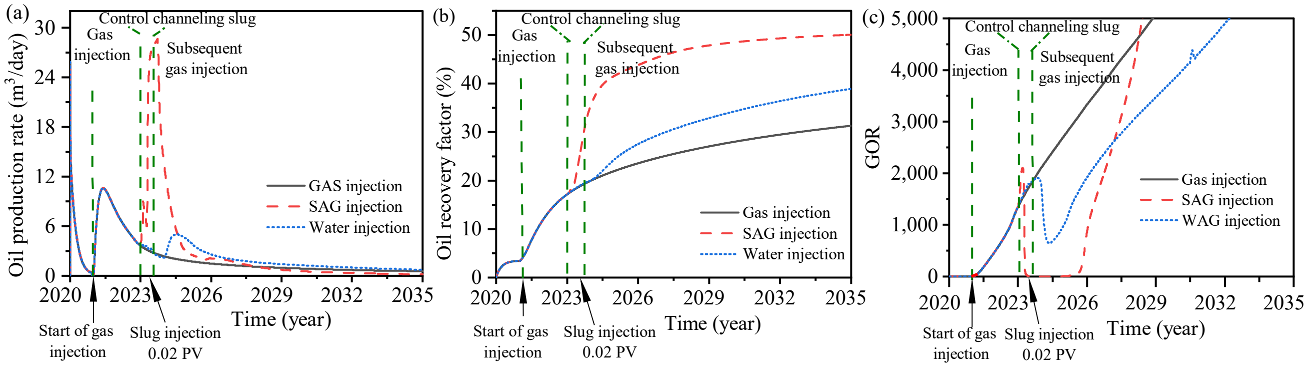

Fig. 15. Effect of development methods on (a) oil production rates, (b) oil recovery factors and (c) GOR.

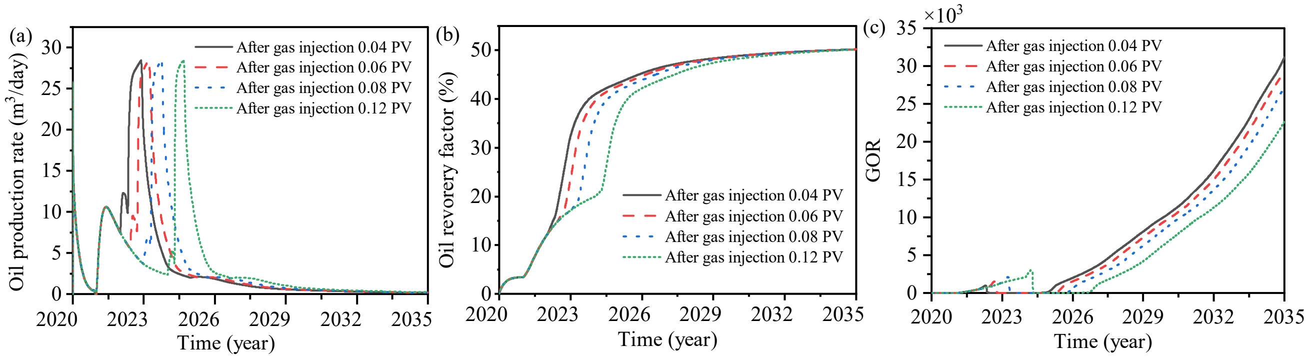

Fig. 16. Effect of foam injection timings on (a) oil production rates, (b) oil recovery factors and (c) GOR.

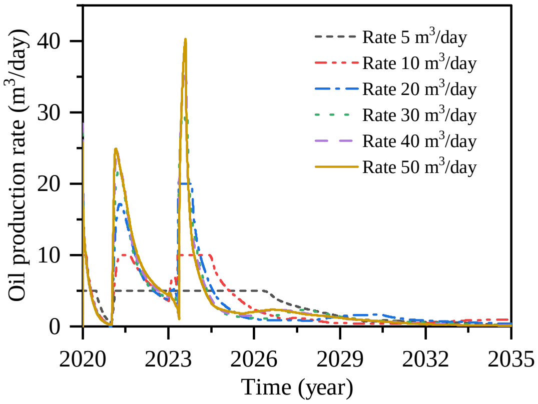

Fig. 17. Oil production rates at different injection rates.

m^3/day and 50 m^3/day achieve similarly high and stable recovery, confirming their effectiveness in maintaining long-term production. The GOR curves as shown in Fig. 18(b) indicate that higher injection rates accelerate the GOR increase, increasing the injection rate beyond 40 m^3/day does not further improve oil recovery but significantly raises GOR. Thus, an injection rate of 40 m^3/day offers the optimal balance between oil recovery and gas mobility control.

4.4.4 Effect of gas-liquid ratios

A sensitivity analysis of gas-liquid ratios in SAG injection is conducted a year after depletion production and 2 years after gas injection. As shown in Fig. 19(a), the oil production rates under gas-liquid ratios of 1 : 1 and 1 : 3 are comparable, while the 1 : 2 ratio leads to a rapid increase in oil production rates after injecting 0.02 PV of foam slug, reaching a peak rate of 3.8 m^3/day and maintaining a high level for about 3 years. In Fig. 19(b), GOR declines by about 77% following foam injection for the 1 : 1 and 1 : 3 ratios, whereas the 1 : 2 ratio immediately reduces the GOR to 0 and maintains gas mobility control for up to 7 years. This is because higher gas-liquid ratios enable early oil production but may reduce foam stability due to excessive capillary pressure, leading to foam collapse and consequently to lower sweep efficiency. Lower gas-liquid ratios produce insufficient foam, weakening the plugging effect and thus reducing oil recovery. In conclusion, a gas-liquid ratio of 1 : 2 provides optimal performance by ensuring adequate foam generation, making it particularly suitable for enhanced oil recovery in low-permeability and tight reservoirs.

4.4.5 Effect of hybrid injection strategies

To reduce operational costs, a hybrid injection strategy is proposed by partially replacing WAG slugs with foam slugs. This approach retains WAG as the main method with partial integration of SAG method. Sensitivity analysis is performed a year after depletion production and 2 years of gas injection. As shown in Fig. 20, both the SAG + 2WAG (i.e., a SAG cycle followed by 2 WAG cycles) and the SAG + WAG + WAG strategies achieve the highest ultimate oil recovery of approximately 50.15%. Looking deeper into the changes in oil recovery during the mid-development stage, one can observe that the recovery factors of these 2 strategies are similar. By

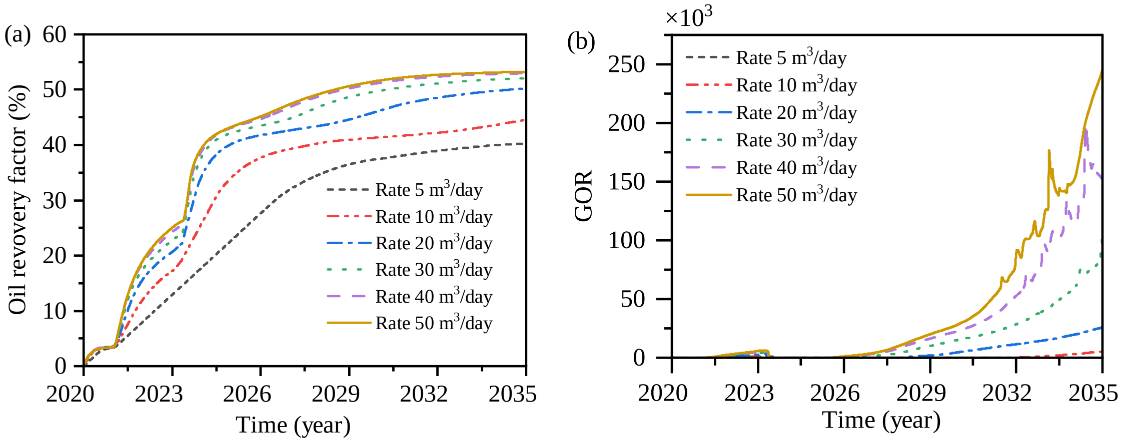

Fig. 18. Effect of injection rates on (a) oil recovery factors and (b) GOR.

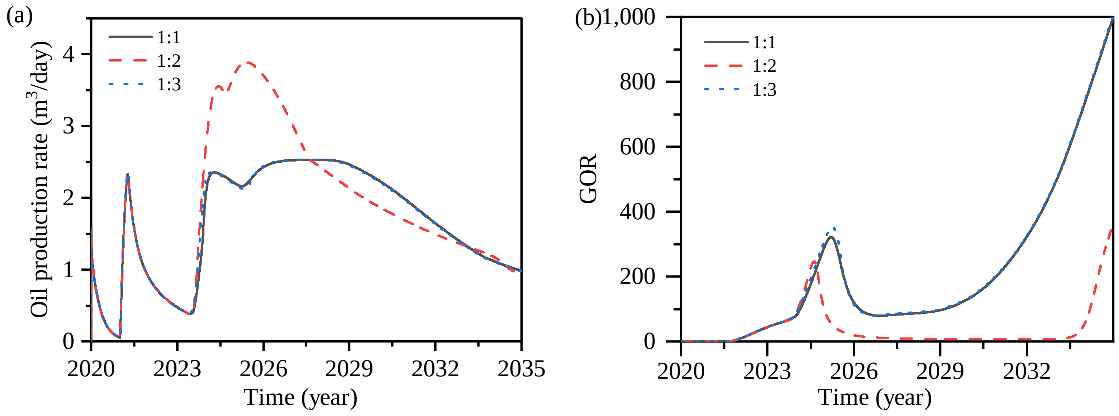

Fig. 19. Effect of gas-liquid ratios on (a) oil production rate and (b) GOR.

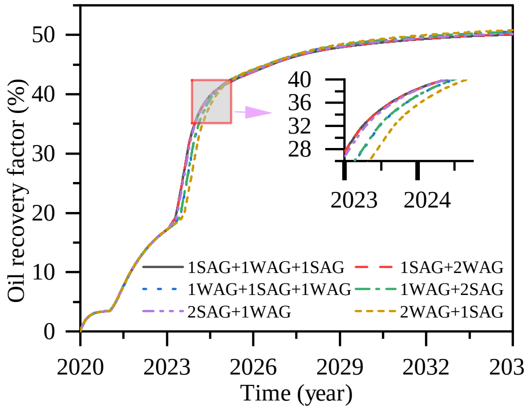

Fig. 20. Oil recovery factors of hybrid injection strategies.

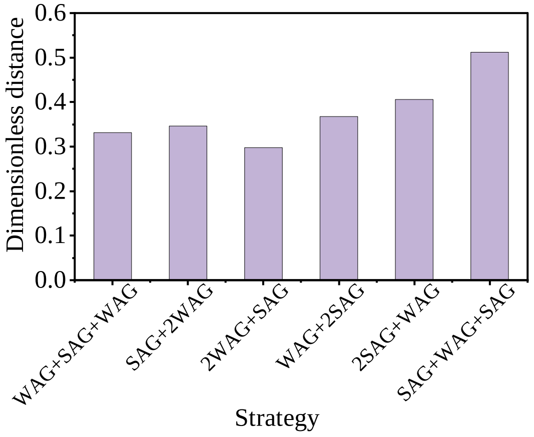

Fig. 21. Dimensionless distances of foam propagation.

comparing the dimensionless distance of foam propagation (Fig. 21), without a preceding SAG slug, the foam exhibits limited propagation ability. Introducing a SAG slug at an early-stage delays gas channeling but results in poor injectivity. Conversely, placing the SAG slug at a later stage improves injectivity and allows foam to penetrate into deeper regions penetration, despite later gas control. Among all cases, the SAG + WAG + WAG strategy demonstrates the most effective foam propagation and oil recovery.

5. Conclusions

This study develops a novel foaming agent (RO-SE) with satisfactory regenerative capability and evaluates its performance across both bulk and interfacial scales. Key flow parameters relevant to CO_2 foam flooding are predicted using pore network modeling integrated into the commercial reservoir simulator (CMG-STARS) to evaluate the performances at reservoir-scale. Specific conclusions are as follows:

1) Foaming agent (RO-SE) exhibits exceptional foaming performance under harsh reservoir conditions, with the V_f and $t_{1/2}$ showing smaller reductions of approximately 37% and 24% in the presence of oil, whereas the conventional foaming agent (SF1) shows more pronounced reductions of 65% and 52%.
2) The interfacial dilational modulus of RO-SE foam system reaches 37.28 mN/m, significantly higher than SF1 (∼28.15 mN/m) and SF2 (∼15.10 mN/m), indicating stronger interfacial rigidity.
3) Pore network simulations reveal that foam has a minimal impact on liquid-phase relative permeability but substantially reduces gas-phase relative permeability by promoting *in-situ* gas trapping.
4) A reservoir-scale simulation method for CO_2 foam flooding grounded from pore-scale performance is developed. The optimal development strategy involved SAG injection with delayed foam deployment, a gas-liquid ratio of 1 : 2, an injection rate of 40 m^3/day, and the SAG + WAG + SAG sequencing, yielding final oil recoveries of 50.06% for SAG injection and 50.15% for SAG + WAG +SAG strategy.

Acknowledgements

The authors are grateful for funding from the National Natural Science Foundation of China (Nos. 52304020 and 12302329), the Natural Science Foundation of Jiangsu Province (No. BK20230622), the Science & Technology Program of Changzhou (No. CJ20235035).

Conflict of interest

The authors declare no competing interest.

References

An, S., Yao, J., Yang, Y., et al. Influence of pore structure parameters on flow characteristics based on a digital rock and the pore network model. Journal of Natural Gas Science and Engineering, 2016, 31: 156-163.

Blunt, M. J., Bijeljic, B., Dong, H., et al. Pore-scale imaging and modelling. Advances in Water Resources, 2013, 51: 197-216.

Cai, J., Jin, T., Kou, J., et al. Lucas-Washburn equation-based modeling of capillary-driven flow in porous systems. Langmuir, 2021, 37(5): 1623-1636.

Cai, J., Sun, S., Wang, H. Current advances in capillarity: Theories and applications. Capillarity, 2023, 7(2): 25-31.

Cai, L., Wu, J., Zhang, M., et al. Investigating the potential of CO_2 nanobubble systems for enhanced oil recovery in extra-low-permeability reservoirs. Nanomaterials, 2024, 14(15): 1280.

Chen, H., Wei, B., Zhou, X., et al. Theory and technology of enhanced oil recovery by gas and foam injection in complex reservoirs. Advances in Geo-Energy Research, 2025, 15(3): 181-184.

Chen, M., Rossen, W., Yortsos, Y. C. The flow and displacement in porous media of fluids with yield stress. Chemical Engineering Science, 2005, 60(15): 4183-4202.

Dubey, S., Majumder, S. K. Stability analysis of CO_2 microbubble for CO_2 sequestration and mobility control in enhanced oil recovery. Chemical Engineering Journal, 2024, 500: 156595.

Hamza, A., Hussein, I. A., Al-Marri, M. J., et al. CO_2 enhanced gas recovery and sequestration in depleted gas reservoirs: A review. Journal of Petroleum Science and Engineering, 2021, 196: 107685.

Ji, B., Fang, J. An overview of efficient development practices at low permeability sandstone reservoirs in China. Energy Geoscience, 2023, 4(3): 100179.

Kharabaf, H., Yortsos, Y. C. Pore network model for foam formation and propagation in porous media. SPE Journal, 1998, 3(1): 42-53.

Kumar, S., Mandal, A. A comprehensive review on chemically enhanced water alternating gas/CO_2 (CEWAG) injection for enhanced oil recovery. Journal of Petroleum Science and Engineering, 2017, 157: 696-715.

Laidlaw, W. G., Wilson, W. G., Coombe, D. A. A lattice model of foam flow in porous media: A percolation approach. Transport in Porous Media, 1993, 11(2): 139-159.

Lin, Z., Kuang, Y., Li, W., et al. Research status and prospects of CO_2 geological sequestration technology from onshore to offshore: A review. Earth-Science Reviews, 2024, 258: 104928.

Li, X., Yang, Z., Li, S., et al. Reservoir characteristics and effective development technology in typical low-permeability to ultralow-permeability reservoirs of China National Petroleum Corporation. Energy Exploration & Exploitation, 2021, 39(5): 1713-1726.

Ma, G., Gong, Q., Xu, Z., et al. The interfacial dilational rheology of surfactant solutions with low interfacial tension. Molecules, 2025, 30(3): 447.

Meakin, P., Tartakovsky, A. M. Modeling and simulation of pore-scale multiphase fluid flow and reactive transport in fractured and porous media. Reviews of Geophysics, 2009, 47(3): 2008RG000263.

Prakash, S., Joshi, D., Ojha, K., et al. Enhanced oil recovery using polymer alternating CO_2 gas injection: Mechanisms, efficiency, and environmental benefits. Energy & Fuels, 2024, 38(7): 5676-5689.

Qin, C., van Brummelen, H. A dynamic pore-network model for spontaneous imbibition in porous media. Advances in Water Resources, 2019, 133: 103420.

Rahman, A., Shirif, E., Torabi. F. Nanoparticle-stabilized CO_2 foam flooding for enhanced heavy oil recovery: A micro-optical analysis. Petroleum, 2024, 10(4): 696-704.

Rasmussen, L., Fan, T., Rinehart, A., et al. Carbon storage and enhanced oil recovery in Pennsylvanian Morrow Formation clastic reservoirs: Controls on oil-brine and oil-CO_2 relative permeability from diagenetic heterogeneity and evolving wettability. Energies, 2019, 12(19): 3663.

Ravera, F., Loglio, G., Kovalchuk, V. I. Interfacial dilational rheology by oscillating bubble/drop methods. Current Opinion in Colloid & Interface Science, 2010, 15(4): 217-228.

Roslin, A., Pokrajac, D., Wu, K., et al. 3D pore system reconstruction using nano-scale 2D SEM images and pore size distribution analysis for intermediate rank coal matrix. Fuel, 2020, 275: 117934.

Xu, T., Tian, H., Zhu, H., et al. China actively promotes CO_2 capture, utilization and storage research to achieve carbon peak and carbon neutrality. Advances in Geo-Energy Research, 2022, 6(1): 1-3.

Yang, J., Zhao, J., Zeng, F. Modeling foam propagation in pore network with designated pressure constraints. Fuel, 2023a, 331: 125772.

Yang, Z., Sun, Q., Deng, H. Multi-scenario modeling and estimating of carbon intensity in China's CO_2-EOR oilfields. Petroleum Science Bulletin, 2023b, 8(2): 247-258. (in Chinese)

Youssif, M. I., Piri, M., Goual, L. Review on foam-assisted gas injection in fractured carbonates for enhanced oil recovery. Energy & Fuels, 2024, 38(17): 15887-15912.

Zhang, C., Wang, P., Song, G. Study on enhanced oil recovery by multi-component foam flooding. Journal of Petroleum Science and Engineering, 2019, 177: 181-187.

Zhang, Y., Liu, Q., Ye, H., et al. Nanoparticles as foam stabilizer: Mechanism, control parameters and application in foam flooding for enhanced oil recovery. Journal of Petroleum Science and Engineering, 2021, 202: 108561.

Zhang, Y., Wang, Y., Xue, F., et al. CO_2 foam flooding for improved oil recovery: Reservoir simulation models and influencing factors. Journal of Petroleum Science and Engineering, 2015, 133: 838-850.

Zhang, Y., Yang, S., Bi, L., et al. A technical review of CO_2 flooding sweep-characteristics research advance and sweep-extend technology. Petroleum Science, 2025, 22(1): 255-276.

Zhao, J., Liu, Y., Qin, F., et al. Pore-scale fluid flow simulation coupling lattice Boltzmann method and pore network model. Capillarity, 2023a, 7(3): 41-46.

Zhao, J., Torabi, F., Yang, J. Role of viscous forces in foam flow in porous media at the pore level. Industrial & Engineering Chemistry Research, 2021, 60(7): 3156-3173.

Zhao, J., Yang, J., Zeng, F. Complex displacement behavior during foaming gas drainage in 2D microfluidic networks. Fuel, 2023b, 344: 128071.

Zhou, G., Li, Y., Liu, Y., et al. Preparation of environment-friendly gel-protein foam and its fire suppression performance for lithiumion batteries. Fuel, 2025, 384: 133979.